JOURNAL OF THEORETICAL AND APPLIED MECHANICS
60, 3, pp. 409-422, Warsaw 2022
https://doi.org/10.15632/jtam-pl/150239

NUMERICAL SIMULATION OF THE PARTICLE SETTLING IN A BINGHAM FLUID USING THE TWO-WAY COUPLING CFD-DEM SCHEME

Joviano Janjar Casarin, Admilson Teixeira Franco, Eduardo Matos Germer, Roderick Gustavo Pivovarski

Federal University of Technology – Paraná (UTFPR), Mechanical Engineering, Curitiba, Paraná, Brazil
e-mail: jovianocasarin@utfpr.edu.br; admilson@utfpr.edu.br; eduardomg@utfpr.edu.br; roderick@alunos.utfpr.edu.br

The computational fluid dynamics coupled with the discrete element method is widely employed to simulate particle-fluid interactions in solid-liquid flows. The restrictions imposed by the CFD-DEM scheme to very fine meshes contribute to a scant amount of numerical results of particle settling in viscoplastic fluids. This paper presents the two-way coupling CFD-DEM simulation of the particle sedimentation in a quiescent Bingham fluid. The results for terminal particle velocity showed good agreement with the experimental data. Owing to the viscoplastic behavior of the fluid, low values of the relaxation parameter of the solid-phase must be specified to obtain accurate results.

Keywords: Bingham model, particle settling, CFD-DEM, two-way coupling

1. Introduction

The behavior of solid particles as they settle in liquid-phases is of particular importance in the modeling of solid-liquid flows. An example is the particle transport in oil wellbore drilling operations using viscoplastic fluids, where the primary purpose is to carry as many particles as possible (Saha *et al.*, 1992). Depending on the flow conditions and particle properties, the gravitational force influences formation of the solid bed, leading to pipe blocking, interruption of the flow, excessive pressure loss and problems due to particle agglomeration (Akhshik *et al.*, 2016).

The non-Newtonian fluids exhibit shear rate-dependent viscosity, meaning that the mathematical modeling is highly complex. The effect of fluid compressibility (Oliveira *et al.*, 2013) further increases complexity of the analysis in some applications. As the fluidization behavior of the liquid-phase demands proper characterization, the numerical modeling of particle settling in polymeric fluids deserves particular attention. Among the numerical methods to conduct simulations of solid-liquid flows, the coupling between the computational fluid dynamics and the discrete element method (CFD-DEM) is convenient to model particle interactions with adjacent particles and solid boundaries, including the flow field structure (Cundall and Strack, 1979).

Usually, the CFD-DEM scheme is employed when many particles take part in the computational domain. However, the adoption of the CFD-DEM to simulate the settling of a single-particle is fundamental to verify capability of the method to reproduce the phenomena that occur in the flow field of viscoplastic fluids. The CFD-DEM is considered a more favorable scheme regarding numerical accuracy and computational requirement when compared with direct numerical simulation (DNS) and coarse-grained methods (Cocco *et al.*, 2017). In the DEM formulation, it is possible to consider the particle size and density distribution in simulations, moreover, the parameters that influence interactions among the particles and solid boundaries (Tsuji *et al.*, 1993).

The CFD-DEM with two-way coupling is useful when the interactions between the particles and the fluid influence the flow field behavior. The Eulerian-Lagrangian approach comprises a discrete description of the particle and a continuous delineation of the liquid-phase (Deen *et al.*, 2007). The viscosity of the Generalized Newtonian Fluids depends on the magnitude of the second invariant of the rate of the strain tensor (Bird *et al.*, 1983). Thus, one can presume that the two-way coupling scheme is essential for the numerical modeling of the solid-liquid flow with viscoplastic fluids.

There are worthwhile studies concerning the numerical modeling of particle sedimentation. Nonetheless, one can observe a shortage of CFD-DEM simulations of particle settling in viscoplastic fluids. Presumably, the lack of data is due to limitations of the method. The cell volume of the mesh must be larger than the particle volume. This restriction induces inaccurate results for particles with a considerable diameter. In addition, the strong interaction between the solid and viscoplastic liquid-phase contributes to instabilities in the CFD-DEM numerical solver. Thus, it is necessary to employ an under-relaxation parameter of the two-way coupling scheme after a proper analysis in this paper. In this context, this paper seeks to present procedures that provide feasible results from simulations of a single spherical particle in a quiescent Bingham fluid, considering the two-way coupling CFD-DEM scheme and the two-grid formulation available in STAR-CCM+ software (CD-Adapco, 2018). The validation of the numerical scheme occurs through the experimental results for the particle settling in a Bingham fluid (Valentik and Whitmore, 1965).

2. Mathematical and numerical modeling

2.1. Fluid rheology

The behavior of viscoplastic fluids is such that the deformation of fluid elements occurs after exceeding a specific yield stress level. The continuous phase considered in this work is a generalized Newtonian Bingham fluid. The constitutive form of the two-parameter Bingham model gives the deviatoric part of the stress tensor $\boldsymbol{\tau}$ according to Eq. (2.1) (Macosko, 1994)

$$\boldsymbol{\tau} = 2\Big(\mu_0 + \frac{\tau_0}{\sqrt{|II_{\mathbf{2D}}|}}\Big)\mathbf{D} \qquad \text{for} \qquad |II_\tau| > \tau_y^2 \tag{2.1}$$

where $\mathbf{D}$ is the rate of the strain tensor according to Eq. (2.2), II_τ the second invariant of the stress tensor, Eq. $(2.3)_1$, τ_0 the fluid yield stress, μ_0 the plastic viscosity of the Bingham fluid, $II_{\mathbf{2D}}$ the second invariant of the rate of the strain tensor, Eq. $(2.3)_2$

$$\mathbf{D} = \frac{1}{2}[\nabla \mathbf{u}_f + (\nabla \mathbf{u}_f)^{\mathrm{T}}] \tag{2.2}$$

and where $\mathbf{u}_f$ is the fluid velocity vector

$$II_{\boldsymbol{\tau}} = \frac{1}{2}[(\,\mathrm{tr}\,\boldsymbol{\tau})^2 - \,\mathrm{tr}\,\boldsymbol{\tau}^2] \qquad II_{\mathbf{2D}} = \frac{1}{2}[(\,\mathrm{tr}\,2\mathbf{D})^2 - \,\mathrm{tr}\,(2\mathbf{D})^2] \tag{2.3}$$

The yield stress τ_0 is a feature of Bingham fluids that influences the behavior of the liquid-phase. The yield stress is the fundamental characteristic when the material is in a structured state. When the material flows, the dynamic yield stress becomes the meaningful aspect. The Bingham number is the ratio between the plastic and viscous effects according to (Bird *et al.*, 1983)

$$\mathrm{Bn} = \frac{\tau_0 d_p}{\mu_0 |\mathbf{u}_f - \mathbf{u}_p|} \tag{2.4}$$

The Hedström number in Eq. (2.5) represents the ratio of yield-inertia effects to viscous stresses and characterizes the behavior of viscoplastic fluids as it combines plastic viscosity and yield stress in a single parameter

$$\mathrm{He} = \frac{\rho_f \tau_0 d_p^2}{\mu_0^2} \tag{2.5}$$

The Bingham fluid is in an unyielded condition $\sqrt{II_{2\mathbf{D}}} = 0$ for $|II_\tau| \leqslant \tau_0^2$, and there is a lack of smoothness in the transition between the yielded and unyielded behavior of the material, leading to inaccurate results at low strain rates. The following dual-viscosity model is considered an excellent approximation for the Bingham apparent viscosity function to be used in numerical modeling of the fluid flow (Beverly and Tanner, 1989)

$$\eta(\dot{\boldsymbol{\gamma}}) = \begin{cases} \eta_r & \text{for} \quad \sqrt{|II_{2\mathbf{D}}|} \leqslant \dot{\gamma}_c \\ \mu_0 + \dfrac{\tau_0\left(1 - \dfrac{\mu_0}{\eta_r}\right)}{\sqrt{|II_{2\mathbf{D}}|}} & \text{for} \quad \sqrt{|II_{2\mathbf{D}}|} > \dot{\gamma}_c \end{cases} \tag{2.6}$$

where η_r is the reference viscosity, and $\dot{\gamma}_c$ the critical shear rate. The dual-viscosity model requires the viscosity η_r as large as possible to develop a critical shear rate as small as possible (Glowinski and Wachs, 2011). It is necessary to mention that Eq. (2.6) incorporates a slight modification used by STAR-CCM+ (CD-Adapco, 2018) when compared to its original form. Numerical studies of the Bingham fluid flow suggest that η_r must be equal or higher than $10^4\mu_0$ to avoid problems with misleading velocity fields originated when using the biviscosity model of Eq. (2.6). The stress tensor is given by

$$\boldsymbol{\tau} = 2\eta(\dot{\boldsymbol{\gamma}})\mathbf{D} \tag{2.7}$$

As it is not possible to model the absolute fluid rigidity, the critical shear rate $\dot{\gamma}_c$ can be used to describe the stress in unyielded regions according to (Prashant and Derksen, 2011)

$$\dot{\gamma}_c = \frac{\tau_0}{\eta_r - \mu_0} \tag{2.8}$$

The average shear rate $\dot{\gamma}_p$ is defined considering the motion of a solid sphere into the liquid phase over the entire particle surface, according to (Lali *et al.*, 1989)

$$\dot{\gamma}_p = \frac{|\mathbf{u}_f - \mathbf{u}_p|}{d_p} \tag{2.9}$$

where $\mathbf{u}_p$ is the particle settling velocity vector, and d_p the particle diameter.

2.2. Forces on a particle under settling conditions

Figure 1 illustrates the sketch of a spherical particle settling in a quiescent fluid. The gravitational force $\mathbf{F}_g$ that acts on the particle is given by

$$\mathbf{F}_g = \rho_p V_p \mathbf{g} \tag{2.10}$$

and is counteracted by the buoyancy force $\mathbf{F}_b$ according to

$$\mathbf{F}_b = -\rho_f V_p \mathbf{g} \tag{2.11}$$

where ρ_p and ρ_f are the particle and fluid densities, respectively, $\mathbf{g}$ is the vector of gravitational acceleration, and V_p is the particle volume.

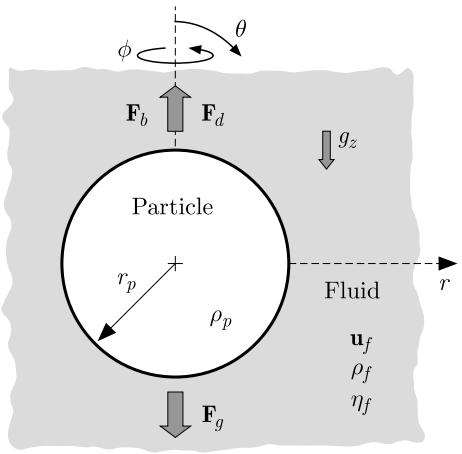

Fig. 1. Forces on a settling spherical particle

The resistance force on the particle is the summation of the pressure and friction drag given by

$$\mathbf{F}_d = \frac{1}{2}\rho_f C_d A_p |\mathbf{u}_f - \mathbf{u}_p|(\mathbf{u}_f - \mathbf{u}_p) \tag{2.12}$$

where C_d is the particle drag coefficient, and A_p is the normal projection of the particle area to the direction of the fluid velocity. The correlation given in Eq. (2.13) was implemented in the software to calculate the drag coefficient on the particle for the Bingham fluid (Dedegil, 1987)

$$C_d = \begin{cases} \dfrac{24}{\mathrm{Re}_{p,\mathrm{Bn}}} & \text{for} \quad \mathrm{Re}_{p,\mathrm{Bn}} \leqslant 8 \\ \dfrac{22}{\mathrm{Re}_{p,\mathrm{Bn}}} + \frac{1}{4} & \text{for} \quad 8 < \mathrm{Re}_{p,\mathrm{Bn}} \leqslant 150 \\ 0.4 & \text{for} \quad \mathrm{Re}_{p,\mathrm{Bn}} > 150 \end{cases} \tag{2.13}$$

where $\mathrm{Re}_{p,\mathrm{Bn}}$ represents the particle Reynolds number for the Bingham fluid according to

$$\mathrm{Re}_{p,\mathrm{Bn}} = \frac{\rho_f |\mathbf{u}_f - \mathbf{u}_p|^2}{\tau_0 + \dot{\gamma}_p \mu_0} \tag{2.14}$$

Equation (2.14) is a satisfactory choice because the fluid yield stress is present in the modeling. It is essential to define that inertial effects are negligible for $\mathrm{Re}_{p,\mathrm{Bn}} \ll 1$, on the other hand, when $\mathrm{Re}_{p,\mathrm{Bn}} \gg 1$, the inertial effects dictate the flow behavior (Thompson and Soares, 2016).

2.3. Discrete element method formulation

The DEM scheme describes the solid-phase motion through the explicit numerical scheme that considers the interactions between particles and solid boundaries for each contact pair, where Newton's second law is employed to model the movement of the solid-phase. The linear and angular momentum balance equations of the particle are (Cundall and Strack, 1979)

$$m_p \frac{d}{dt}\mathbf{u}_p = -V_p \nabla p + \mathbf{F}_C + \mathbf{F}_B + \mathbf{F}_{SL} \qquad \mathbf{I}_p \frac{d}{dt}\boldsymbol{\omega}_p = \mathbf{T}_p \tag{2.15}$$

where m_p is the particle mass, p – pressure, $\mathbf{F}_C$ – contact forces among particles and solid boundaries (not considered in this paper, as a single particle is injected in the domain and there are no interactions with solid boundaries), $\mathbf{F}_B$ – body forces acting on the particle, $\mathbf{F}_{SL}$ – interaction forces between the solid and liquid phases – the drag force from Eq. (2.12), $\mathbf{I}_p$ is the particle moment of inertia, $\boldsymbol{\omega}_p$ – particle angular velocity, and $\mathbf{T}_p$ any torque on the particle.

2.4. Balance equations of the continuum phase

For the liquid-phase an incompressible fluid is assumed and the differential equations for the mass and momentum balance are

$$\rho_f \frac{\partial}{\partial t} C_f + \nabla \cdot \rho_f (C_f \mathbf{u}_f) = 0 \tag{2.16}$$

and

$$\rho_f \frac{\partial}{\partial t} (C_f \mathbf{u}_f) + \rho_f (C_f \mathbf{u}_f \cdot \nabla \mathbf{u}_f) = -(C_f \nabla p) + (\nabla \cdot C_f \boldsymbol{\tau}) + C_f \rho_f \mathbf{g} + \mathbf{M}_{imt} \tag{2.17}$$

where C_f is the volume fraction of the liquid-phase, $\boldsymbol{\tau}$ – viscous stress tensor, and $\mathbf{M}_{imt}$ the interphase momentum transfer, Eq. (2.18) (Crowe *et al.*, 2012). The volume fraction of the solid phase is C_s. It follows that $C_f = 1 - C_s$. The interphase momentum transfer $\mathbf{M}_{imt}$ in Eq. (2.17) represents the summation of the interaction forces $\mathbf{F}_{SL}$ on the solid-phase S due to the liquid phase L in each fluid cell volume V, and given by

$$\mathbf{M}_{imt} = \sum_{V} \mathbf{F}_{SL} \tag{2.18}$$

The interaction force $\mathbf{F}_{SL}$ in Eq. (2.18) can be interpreted as the drag force $\mathbf{F}_d$ on the particle. In the CFD-DEM two-way coupling scheme, the contact forces that the phases exert one on another are calculated using the interphase momentum transfer $\mathbf{M}_{imt}$ as (Crowe *et al.*, 2012)

$$\mathbf{M}_{imt} = \frac{1}{V_{vc}} \sum_{N_p} \mathbf{F}_d \tag{2.19}$$

where V_{vc} is the virtual cell volume, see Fig. 2a, N_p is the number of particles inside any virtual cell.

Figure 2a demonstrates the two-grid model of the CFD-DEM scheme on which the equations expressing the fluid-particle coupling are based. The balance equations of the continuous phase are solved by the finite volume method (Patankar, 1980) and discretized in the fluid cells. The modeling of the solid-phase occurs according to the virtual cell, which contains a group of small fluid cells (Deb and Tafti, 2013). The interaction forces between the solid and liquid-phases are calculated in the virtual cell. The contribution of the momentum is distributed over the fluid cells considering the volume fraction C_f of the liquid phase. The velocity field is calculated on the fluid cell grid and mapped to the virtual cell grid for the interphase momentum exchange, and the solid fraction and momentum interphase exchange terms are calculated on the particle grid (virtual cell) and mapped back to the fluid grid (fluid cell). The parameter cell cluster scale C_{cs} is defined as a multiple of the largest fluid cell length L_{fc}, and employed to find the length of the virtual cell as

$$L_{vc} = C_{cs} L_{fc} \tag{2.20}$$

The volume fraction of the solid phase in the virtual cell is given by

$$C_{s,vc} = \frac{1}{V_{vc}} \sum_{N_p} V_p \tag{2.21}$$

where V_p represents the particle volume. The volume fraction of the solid-phase is high in the fluid cells grid early in the sedimentation, which contributes to solver instability. This instability is related to the perturbation introduced by the elevated value of the interphase momentum

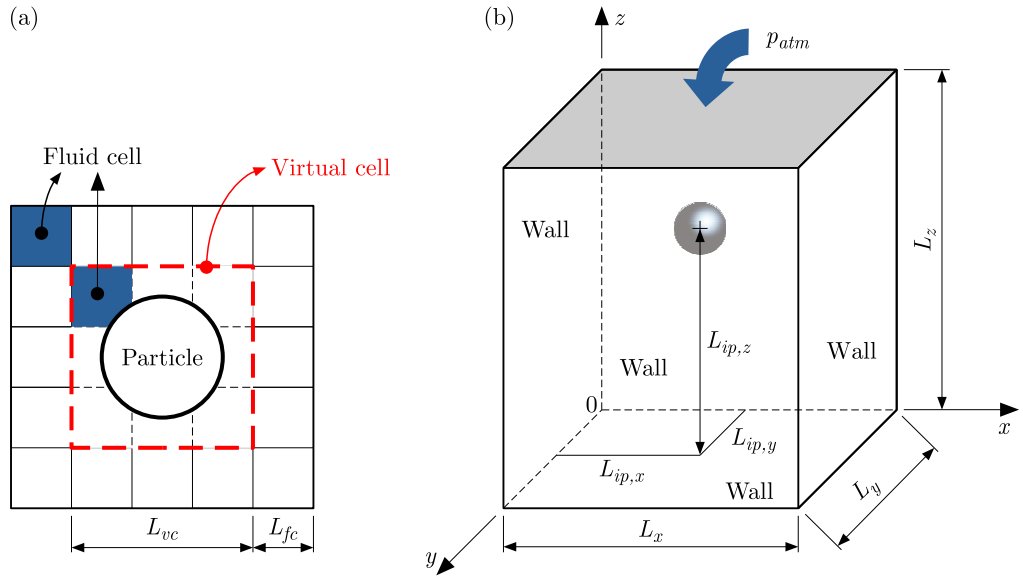

Fig. 2. (a) Two-grid scheme of the CFD-DEM two-way coupling. L_{fc} is the fluid cell size, and L_{vc} is the virtual cell size. (b) Computational domain for numerical simulations of the particle settling

term $\mathbf{M}_{imt}$ and the low volume fraction of the fluid C_f in Eq. (2.17), which are responsible for increasing numerical residuals. The size of this perturbation depends on the level of coupling between the solid and liquid-phases (Kohnen *et al.*, 1994). There is a strong interaction between the solid and liquid-phase in solid-liquid flows with viscoplastic fluids. Therefore, to ensure a feasible solution, the volume fraction of the solid-phase must be relaxed. The α parameter can be employed according to Eq. (2.22) to reduce the particle volume fraction during initial iterations, corresponding to the beginning of the sedimentation

$$C_s^{i+1} = \alpha C_{s,vc}^{i+1} + (1-\alpha) C_s^i \tag{2.22}$$

where α is the under-relaxation factor of the Lagrangian phase (solid phase) $0 \leqslant \alpha \leqslant 1$), $C_{s,vc}^{i+1}$ is the Lagrangian phase volume fraction at the coupling iteration $(i+1)$, and C_s^i is the volume fraction of solid contributed to the continuous phase in the iteration i. The solid volume fraction under the relaxation factor in Eq. (2.22) varies in every iteration. For small values of α, the volume fraction of the solid phase is minimal in the initial iterations, rising to a constant value as the iterations progress.

In the two-grid scheme, the information transfer of the fluid volume fraction from the virtual grid to the fluid grid is given by

$$C_{fc} = \Psi_{vm \to fm}\{C_f\} \tag{2.23}$$

where C_{fc} is the fluid volume fraction of the fluid cells inside the virtual cell, and $\Psi_{vm \to fm}$ is the distribution function from the virtual mesh (vm) to the fluid mesh (fm). In the present study, the mapping function is given by $\Psi_{vm \to fm} = 1$ (Deb and Tafti, 2013), meaning that the same value of the void fraction in the virtual cell is mapped to every fluid cell inside the virtual cell $C_{fc} = C_f$.

2.5. Boundary and initial conditions for the particle settling problem

Figure 2b illustrates the computational fluid domain consisting of a duct with a square cross-section with sides $L_x = L_y$ and height L_z. The square cross-section has been selected so that the

mesh could have finite volumes with regular hexahedral geometry. The mesh with hexahedral volumes produces low numerical diffusivity (Sosnowski *et al.*, 2019). The wall specification incorporates the no-slip condition. The atmospheric pressure acts on the liquid at the top of the computational domain in Fig. 2b. The dimension in the y-direction L_y is the same as in the x-direction L_x. The particle is injected at a point given by the location $L_{ip,x} = 0.5L_x = L_{ip,y} = 0.5L_y$, and in the vertical position $L_{ip,z} = 0.8L_z$. The minimum value of the vertical distance L_z is 1.5 m, and was specified allowing the particle to reach terminal velocity before coming into contact with the bottom wall.

Equation (2.24) represents the boundary and initial conditions for the solid-phase

$$u_{p,x}(x;t=0) = u_{p,y}(y;t=0) = u_{p,z}(z=L_{ip,z};t=0) = 0 \tag{2.24}$$

The boundary and initial conditions for the liquid-phase are given as

$$\begin{aligned} &u_{f,x}(x;t=0) = u_{f,y}(y;t=0) = u_{f,z}(z;t=0) = 0 \\ &u_{f,x}(x=0;t) = u_{f,y}(y=0;t) = u_{f,x}(x=L_x;t) = u_{f,y}(y=L_y;t) = 0 \\ &u_{f,z}(z=0;t) = 0 \end{aligned} \tag{2.25}$$

The pressure specification at the top of the computational domain L_z is the atmospheric pressure

$$p(z=L_z;t) = p_{atm} \tag{2.26}$$

3. Simulation data

The discrete phase consists of a solid and spherical particle with diameter $d_p = 9.5$ mm, and density $\rho_p = 6751\,\mathrm{kg{\cdot}m^{-3}}$. The simulations in the present study consider two fluids with properties according to the experimental data (Valentik and Whitmore, 1965). Fluid 1: $\tau_0 = 25.0$ Pa, $\mu_0 = 6.7{\cdot}10^{-3}$ Pa·s, and $\rho_p/\rho_f = 5.59$; fluid 2: $\tau_0 = 7.8$ Pa, $\mu_0 = 4.0{\cdot}10^{-3}$ Pa·s, and $\rho_p/\rho_f = 5.87$. The chosen value of the reference viscosity η_r in Eq. (2.6) is $\eta_r = 1.0 \cdot 10^4$, according to the numerical results for the Poiseuille flow of the Bingham fluid illustrated in Fig. 3. The velocity profile is better characterized for the condition $\eta_r = 1.0 \cdot 10^4 \mu_0$ and mesh configuration 5.

The size of the computational domain given in Eq. (3.1) has been employed to evaluate the influence of the rigid walls on the numerical results

$$L_{dom} = W_d\, d_p \tag{3.1}$$

where W_d is the parameter of the wall-to-wall distance to the particle-diameter. L_{dom} is defined as L_x in the x-direction and L_y in the y-direction of Fig. 2b. The dimensions of the computational domain range from $L_x = L_y = 47.5$ mm for $W_d = 5$, to $L_x = L_y = 190$ mm for $W_d = 20$.

Table 1 gives the mesh parameters of the fluid and the virtual grid. The grid refinement ratio is 0.75. The balance equations of mass and momentum of the continuous phase were discretized with the finite volume method and the SIMPLE scheme employed in the pressure--velocity coupling (Patankar, 1980). The implicit unsteady solver was selected with the second--order temporal discretization. The point-iterative technique of Gauss-Seidel and the algebraic multigrid method solve the discretized linear system of equations under the convergence criterion of 10^{-4} for all normalized residuals. The influence of the outer iterations in the CFD-DEM coupling was performed considering three orders of magnitude for the fluid time step Δt_f to the particle time step Δt_p ratio given by $\Delta t_f/\Delta t_p = 1$, $\Delta t_f/\Delta t_p = 10$, and $\Delta t_f/\Delta t_p = 100$ (Yao *et al.*, 2020).

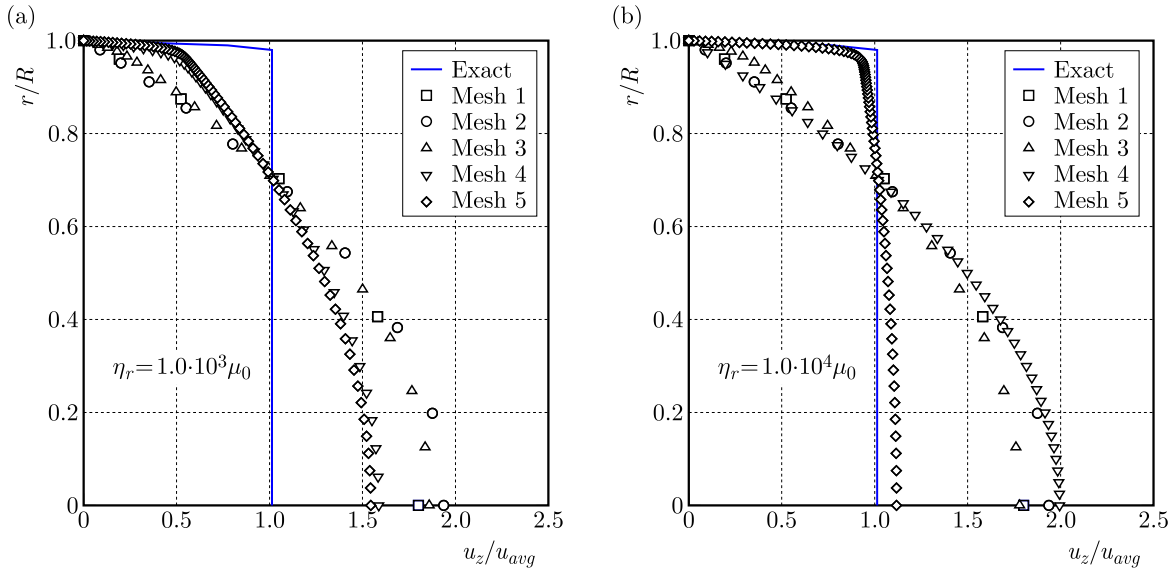

Fig. 3. Poiseuille flow of the Bingham fluid in a circular pipe of radius R for the following conditions: $\rho_f = 1207\,\mathrm{kg{\cdot}m^{-3}}$, $\tau_0 = 25\,\mathrm{Pa}$, $R = 25 \cdot 10^{-3}\,\mathrm{m}$, $dp/dz = 2040\,\mathrm{Pa{\cdot}m^{-1}}$: (a) $\eta_r = 1.0 \cdot 10^3 \mu_0$, (b) $\eta_r = 1.0 \cdot 10^4 \mu_0$

Table 1. Mesh configurations employed in the simulations according to the parameters in Fig. 2a

Mesh	Fluid cell size	Cell cluster scale	Virtual cell size
M_1	$L_{fc} = 0.5 d_p$	$C_{cs} = 3$	$L_{vc} = 3L_{fc}$
M_2	$L_{fc} = 0.375 d_p$	$C_{cs} = 4$	$L_{vc} = 4L_{fc}$
M_3	$L_{fc} = 0.281 d_p$	$C_{cs} = 5$	$L_{vc} = 5L_{fc}$

4. Results and discussion

Figures 4a to 4c illustrate the normalized particle velocity versus time step of the liquid phase for $W_d = 5$ to $W_d = 20$ and mesh configurations M_1 to M_3. As the particle volume is larger than the fluid cell volume, the mesh refinement study must ensure that the volume of the virtual cell is larger than the particle volume by changing the parameter C_{cs}. The examination of Figs. 4a to 4c reveals the wall domain influence on the results, and that the intermediate mesh M_2 ($L_{fc} = 0.375 d_p$) with $C_{cs} = 4.0$, the $W_d = 10$ and the maximum fluid time step $\Delta t_f = 2.0 \cdot 10^{-3}$ s are suitable to yield accurate numerical results for the particle terminal velocity. The maximum error in the particle terminal velocity compared with the experimental values is around $\pm 5\%$, indicating that the two-grid scheme is suitable to model the particle settling in viscoplastic fluids using the two-way coupling CFD-DEM.

It is evident that for simulations with small fluid cell volumes, the numerical results for particle settling velocity are near the experimental data, indicating how the correct choice of the mesh size is essential to obtain accurate numerical results. While simulations of the Bingham fluid flow demand meshes with small volume elements for better characterization of the viscosity function, the CFD-DEM requires that the volume of the fluid cell be greater than the particle volume to reduce numerical instabilities. When the particle volume is greater than the volume of the fluid cell element, the two-grid scheme is suitable for simulating viscoplastic solid-liquid flows. For fine grids, the virtual cell must be larger than the fluid cell to ensure a suitable volume fraction and accurate drag modeling.

Meshes with smaller elements $M_3 < M_2 < M_1$ produce more accurate results when compared with the experimental data for all the values of W_d ratio. The upper and lower limits

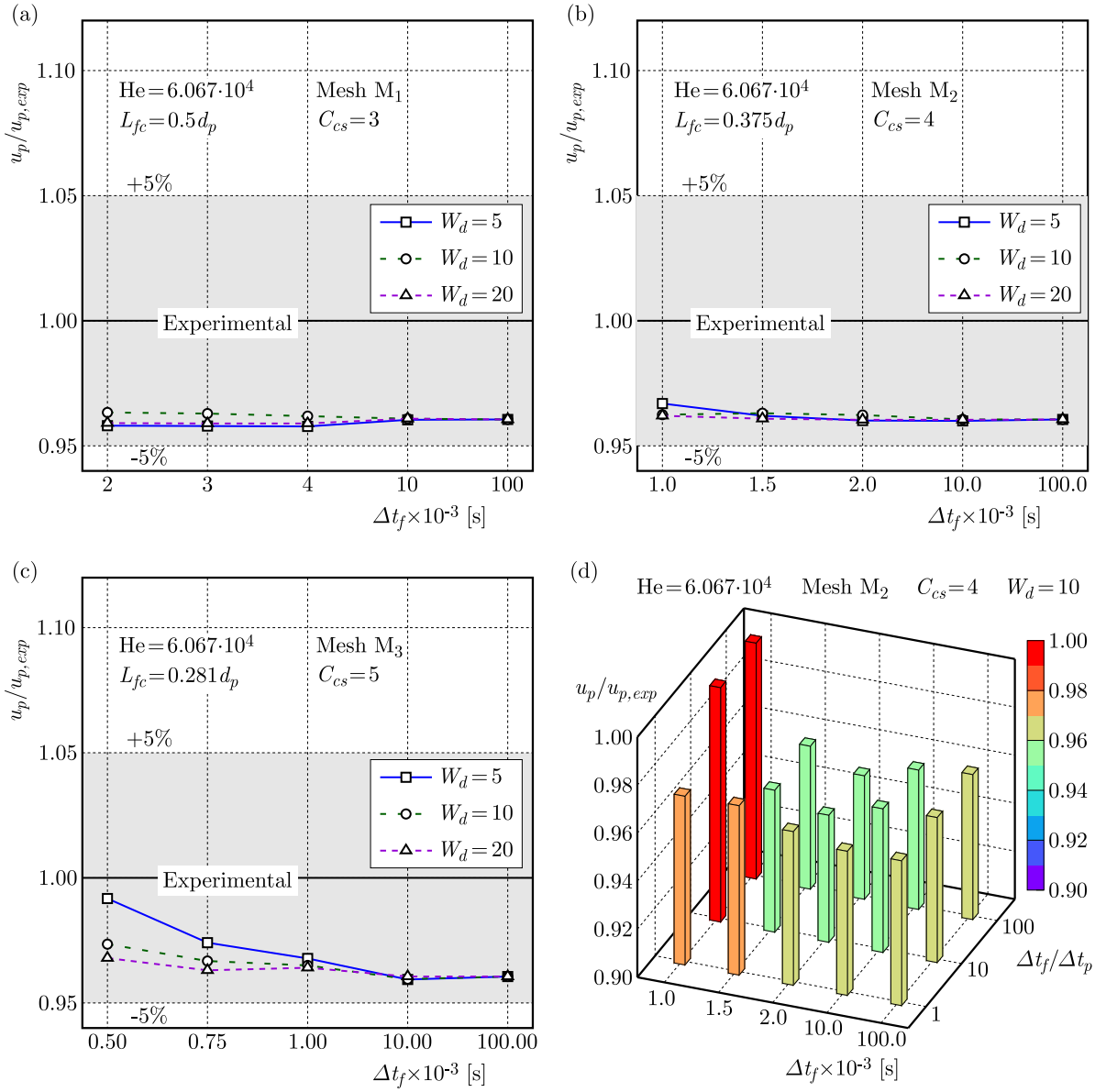

Fig. 4. Normalized particle velocity vs. fluid time step for $\Delta t_f/\Delta t_p = 1$: (a) mesh M_1, (b) mesh M_2, (c) mesh M_3, (d) influence of the outer iterations considering the time step ratio $\Delta t_f/\Delta t_p$

of ±5% represent the maximum relative errors when the numerical results are compared with the normalized experimental value 1.0. The C_{cs} value depends on the fluid mesh size and particle volume, and must consider the void fraction for the liquid phase in the continuous-phase mesh, i.e., the volume occupied by the particle in the fluid cell element.

A likely explanation for finding that the particle velocity increases with mesh refinement is that since viscosity is a function of the strain-rate, a finer mesh characterizes the velocity gradient better, leading to more accurate results, as illustrated in Figs. 4a to 4c. As the numerical results approximate the experimental results when finer meshes are employed with larger values of C_{cs} parameter, the virtual cell length L_{vc} must be carefully specified to ensure satisfactory results in numerical simulations when using meshes with small volume elements. If grid refinement is employed, a larger C_{cs} value is mandatory to increase the virtual cell length so that the shear rate and viscosity function are modeled accurately. The optimum value for the virtual cell length L_{vc} must cover the particle diameter. However, it depends on the fluid cell length by the

C_{cs} parameter. So, the best choice of the virtual cell length is related to the optimum size of the fluid cell length.

The unusual results of the particle velocity for lower W_d values are intriguing in Figs. 4b and 4c. These results represent simulations with smaller grid sizes – meshes M_2 and M_3. Theoretically, the further the distance between the particle surface and rigid boundary walls, the greater the particle terminal velocity should be due to the lesser confinement effect, at least for the Stokes condition (Atapattu *et al.*, 1995). The results obtained in this work show that when the particle is positioned near the wall, the terminal velocity is higher and approaches the experimental value. The possible reason is the extension and proximity of the yielded surface of the fluidized region to the wall. The no-slip condition at the rigid walls plays a significant influence on the fluidized region surrounding the particle and, hence, on the particle terminal velocity.

An important parameter to be analyzed in the CFD-DEM scheme is the coupling level found by using the fluid to particle time step ratio $\Delta t_f/\Delta t_p$. Low values of the $\Delta t_f/\Delta t_p$ denote low efficiency in the CFD-DEM coupling (Yao *et al.*, 2020). Figure 4d illustrates the influence of $\Delta t_f/\Delta t_p$ on the simulation results. If lower values of the fluid time step Δt_f are employed, higher values of $\Delta t_f/\Delta t_p$ – or smaller values for the particle time step Δt_p – are required to generate numerical results nearest the experimental one. This behavior agrees with numerical results in the literature (Yao *et al.*, 2020).

Figure 5a illustrates the behavior of the particle velocity vs. time for $\mathrm{He} = 6.067 \cdot 10^4$ and $\mathrm{Bn} = 52.1$, and in Fig. 5b for $\mathrm{He} = 5.055 \cdot 10^4$ and $\mathrm{Bn} = 14.7$. The under-relaxation factor α of the Lagrangian phase in Eq. (2.22) had a significant influence on the accuracy and numerical stability of the results for values of ranging from $1.0 \cdot 10^{-3}$ to 1.0. The numerical results of the particle velocity exhibit excellent stability for $\alpha < 1.0 \cdot 10^{-2}$.

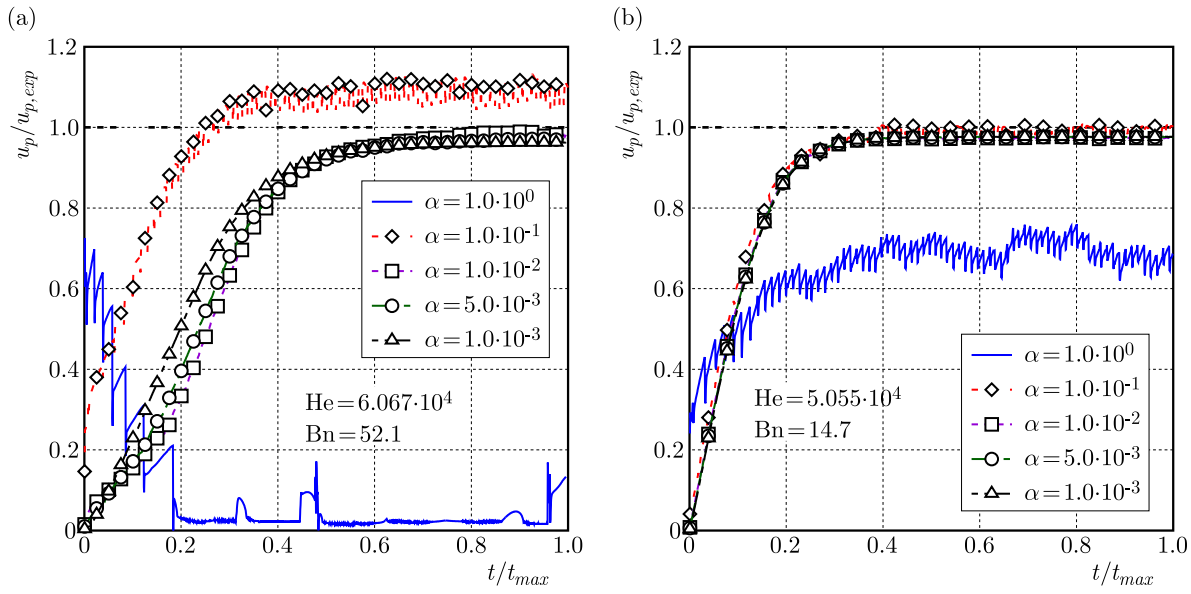

Fig. 5. Particle velocity vs. time for different values of the parameter $W_d = 10$, mesh M_2: (a) $\mathrm{Re}_{p,\mathrm{Bn}} = 21.9$, $\mathrm{Bn} = 52.1$, $\mathrm{He} = 6.067 \cdot 10^4$; (b) $\mathrm{Re}_{p,\mathrm{Bn}} = 219$, $\mathrm{Bn} = 14.7$, $\mathrm{He} = 5.055 \cdot 10^4$. u_p and $u_{p,exp}$ are the numerical and experimental particle velocities, respectively. t_{max} is the maximum simulation time required for the particle to reach the terminal velocity

Inconsistent movements of the particle were observed for $\alpha > 1.0 \cdot 10{-}2$, as shown in Fig. 5. Therefore, to ensure stable simulations, a value of $\alpha = 5.0 \cdot 10^{-3}$ was employed in all numerical analyses. The behavior of the particle velocity versus time agrees qualitatively with the numerical

results obtained in the particle settling study with the Lattice-Boltzmann scheme (Prashant and Derksen, 2011).

The influence of the fluid yield stress on the particle velocity is more apparent for higher values of Bn and α. This can be seen comparing the two Bingham numbers in Fig. 5. The unstable behavior of the particle settling velocity for $\alpha > 1.0 \cdot 10^{-2}$ Fig. 5a is associated with the influence of the fluid yield stress during the particle injection at the beginning of the simulation due to the strong interaction between the solid and liquid-phases (Kohnen *et al.*, 1994). Moreover, it is essential to mention that the specification of smaller values of the under-relaxation parameter $\alpha \leqslant 1.0 \cdot 10^{-3}$ worsens the results of the particle settling velocity. If the α parameter is too small, the volume occupied by the particle in the fluid cells is moderate along time, according to Eq. (2.22). Thus, the body forces acting on the particle are small, affecting the settling velocity. One can infer that the selection of the under-relaxation parameter must not be aleatory, demanding proper analysis.

Figure 6 illustrates the fluid shear stress field, including the yielded and unyielded regions around the particle settling in the Bingham fluid for (a) Bn = 52.1 and (b) Bn = 14.7. The outermost zone around the particle corresponds to the yielded liquid-phase until reaching the limit called yield surface. The normalized isostress line $\tau/\tau_0 = 1.0$ indicates the unyielded condition of the liquid-phase.

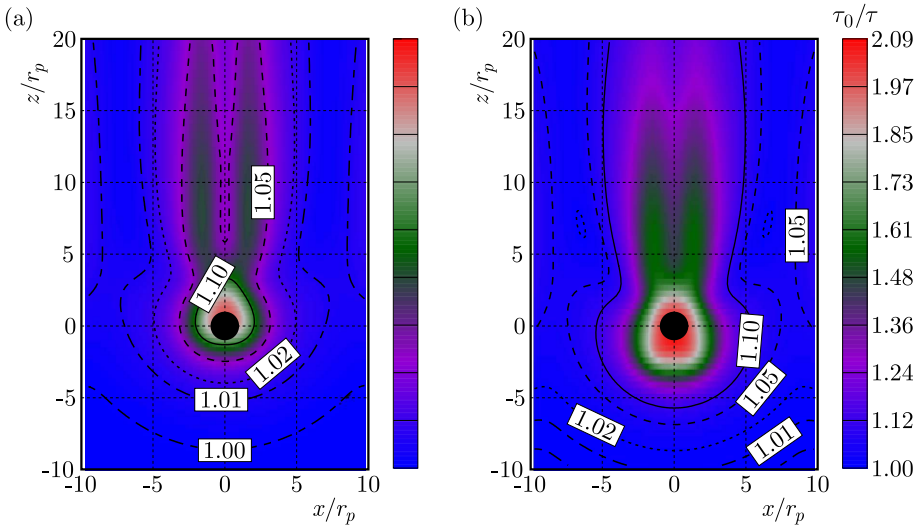

Fig. 6. Shear stress field for $W_d = 10$, mesh M_3, and $\Delta t_f = 1.0 \cdot 10^{-3}$ s: (a) $\mathrm{Re}_{p,\mathrm{Bn}} = 21.9$, Bn = 52.1, $\mathrm{He} = 6.067 \cdot 10^4$; (b) $\mathrm{Re}_{p,\mathrm{Bn}} = 219$, Bn = 14.7, $\mathrm{He} = 5.055 \cdot 10^4$

Figure 7 illustrates the rate of the strain tensor field around the particle that settles in a quiescent Bingham fluid for (a) Bn = 52.1 and (b) Bn = 14.7. The numerical results agree qualitatively well with other numerical data in the literature (Glowinski and Wachs, 2011; Prashant and Derksen, 2011). The fore-aft asymmetry in the strain-rate field is caused by inertial effects. The Stokes number $\mathrm{St} = \rho_p \dot{\gamma} r^2 / 3.5 \mu_0$ represents the ratio of the characteristic kinetic energy of the particle to the characteristic viscous energy associated with motion of the particle through the fluid (Coussot, 2005). For the conditions simulated in this paper, the Stokes number is 122, meaning that the fluid has very limited influence on particle motion.

It is possible to see the influence of the yield stress on the fluidized region encompassing the particle. For the fluid with high yield stress (Bn = 52.1), the extension of the yielded region is minor when observing the distance of the yield surface from the particle limits. The last behavior was also reported in the numerical analysis of particle settling in viscoplastic fluids using the Lattice-Boltzmann scheme (Prashant and Derksen, 2011). The liquid-phase behavior in Fig. 7 agrees with the Bingham fluid theory, which exhibits two distinct responses depending on the

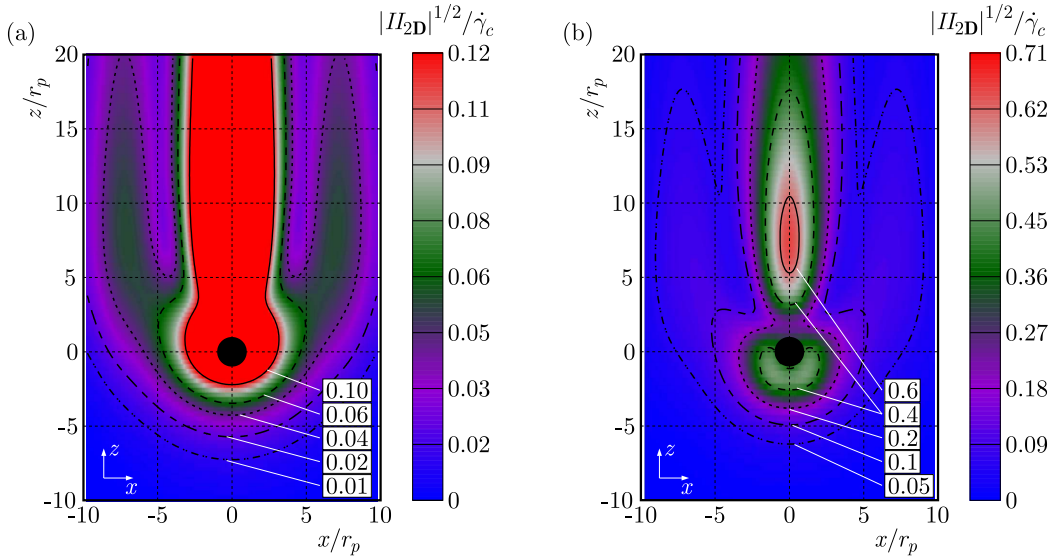

Fig. 7. Strain-rate tensor field for $W_d = 10$, mesh M_3, and $\Delta t_f = 1.0 \cdot 10^{-3}$ s: (a) $\mathrm{Re}_{p,\mathrm{Bn}} = 21.9$, $\mathrm{Bn} = 52.1$, $\mathrm{He} = 6.067 \cdot 10^4$; (b) $\mathrm{Re}_{p,\mathrm{Bn}} = 219$, $\mathrm{Bn} = 14.7$, $\mathrm{He} = 5.055 \cdot 10^4$

magnitude of the strain-rate. For a shear rate lower than the critical value $\dot{\gamma}_c$ in Eq. (2.8), the fluid exhibits solid-like behavior (unyielded) and has a high viscosity value given by as expected from Eq. (2.6). In contrast, in regions with high shear rates, the flow assumes Newtonian behavior (yielded) (Macosko, 1994).

5. Conclusions

The numerical modeling of the particle sedimentation in a Bingham fluid carried out in this paper was successful. The two-way CFD-DEM coupling scheme, including the two-grid approach, proved to be feasible to simulate the solid-liquid flow of a viscoplastic fluid for a particle volume higher than the fluid cell volume. Therefore, it is possible to surpass the mesh size limitation of the CFD-DEM.

Numerical results show that the finer mesh M_3 with fluid cell size $L_{fc} = 0.281 d_p$, and cell cluster scale $C_{cs} = 5$ generates the particle terminal velocity nearer to 1.0, the value corresponding with experimental observations. Nonetheless, it is possible to employ an intermediate mesh configuration $\mathrm{M}_2 - L_{fc} = 0.375 d_p$, and $C_{cs} = 5$ to obtain a compromise between results with high accuracy and low computational effort. One can state that using a low value in the relaxation factor of the solid-phase α is essential to achieve both numerical stability and accuracy in the numerical modeling of particle settling. The condition above is meaningful when there is a substantial interaction between the liquid and solid-phases, characterized by a fluid with high yield stress τ_0.

The size of the computational domain has an insignificant influence on the numerical results for the condition $W_d \geqslant 10$. The yield and unyielded surfaces were recognized in all situations, showing that the two-way coupling CFD-DEM simulation was able to characterize the viscoplastic behavior of the Bingham fluid in the sedimentation problem. The extension of the yielded and unyielded regions agrees qualitatively well with those reported in similar numerical studies. The fore-aft and radial asymmetry in the stress and rate of the strain tensor fields result from dynamic effects due to the moderate particle Reynolds number. In conclusion, CFD-DEM with a two-way coupling scheme is considered suitable for the modeling of the particle settling in a Bingham fluid as long as the precautions discussed in this paper are taken into account.

References

1. Akhshik S., Behzad M., Rajabi M., 2016, CFD-DEM simulation of the hole cleaning process in a deviated well drilling: the effects of particle shape, *Particuology*, **25**, 72-82
2. Atapattu D.D., Chhabra R.P., Uhlherr P.H.T., 1995, Creeping sphere motion in Herschel--Bulkley fluids: flow field and drag, *Journal of Non-Newtonian Fluid Mechanics*, **59**, 245-265
3. Beverly C.R., Tanner R.I., 1989, Numerical analysis of extrudate swell in viscoelastic materials with yield stress, *Journal of Rheology*, **33**, 989-1009
4. Bird R.B., Dai G.C., Yarusso B.J., 1983, The rheology and flow of viscoplastic materials, *Reviews in Chemical Engineering*, **1**, 1-70
5. CD-Adapco, 2018, Simcenter STAR-CCM+ User Guide, Siemens PLM Software
6. Cocco R., Fullmer W.D., Liu P., Hrenya C.M., 2017, CFD-DEM modeling the small to understand the large, *Chemical Engineering Progress*, **113**, 38-45
7. Coussot P., 2005, *Rheometry of Pastes, Suspensions, and Granular Materials: Applications in Industry and Environment*, John Wiley & Sons, Inc., Hoboken, NJ, USA
8. Crowe C.T., Schwarzkopf J.D., Sommerfeld M., Tsuji Y., 2012, *Multiphase Flows with Droplets and Particles*, 2nd ed. CRC Press
9. Cundall P.A., Strack O.D.L., 1979, A discrete numerical model for granular assemblies, *Géotechnique*, **29**, 47-65
10. Deb S., Tafti D.K., 2013, A novel two-grid formulation for fluid-particle systems using the discrete element method, *Powder Technology*, **246**, 601-616
11. Dedegil M.Y., 1987, Drag coefficient and settling velocity of particles in non-Newtonian suspensions, *Journal of Fluids Engineering*, **109**, 319-323
12. Deen N.G.,Van Sint Annaland M., Van der Hoef M.A., Kuipers J.A.M., 2007, Review of discrete particle modeling of fluidized beds, *Chemical Engineering Science*, **62**, 28-44
13. Glowinski R., Wachs A., 2011, On the numerical simulation of viscoplastic fluid flow, [In:] *Handbook of Numerical Analysis*, Elsevier, 483-717
14. Kohnen G., Rüger M., Sommerfeld M., 1994, Convergence behaviour for numerical calculations by the Euler/Lagrange method for strongly coupled phases, *ASME-PUBLICATIONS-FED*, **185**, 191-202
15. Lali A.M., Khare A.S., Joshi J.B., Nigam K.D.P., 1989, Behaviour of solid particles in viscous non-Newtonian solutions: settling velocity, wall effects and bed expansion in solid-liquid fluidized beds, *Powder Technology*, **57**, 39-50
16. Macosko C.W., 1994, *Rheology Principles, Measurements, and Applications. Advances in Interfacial Engineering Series*, VCH, New York
17. Oliveira G.M., Franco A.T., Negrão C.O.R., Martins A.L., Silva R.A., 2013, Modeling and validation of pressure propagation in drilling fluids pumped into a closed well, *Journal of Petroleum Science and Engineering*, **103**, 61-71
18. Patankar S.V., 1980, *Numerical Heat Transfer and Fluid Flow. Series in Computational Methods in Mechanics and Thermal Sciences*, Hemisphere Pub. Corp., McGraw-Hill, Washington, New York
19. Prashant, Derksen J.J., 2011, Direct simulations of spherical particle motion in Bingham liquids, *Computers and Chemical Engineering*, **35**, 1200-1214
20. Saha G., Purohit N.K., Mitra A.K., 1992, Spherical particle terminal settling velocity and drag in Bingham liquids, *International Journal of Mineral Processing*, **36**, 273-281
21. Sosnowski M., Gnatowska R., Sobczyk J., Wodziak W., 2019, Computational domain discretization for CFD analysis of flow in a granular packed bed, *Journal of Theoretical and Applied Mechanics*, **57**, 833-842

22. Thompson R.L., Soares E.J., 2016, Viscoplastic dimensionless numbers, *Journal of Non--Newtonian Fluid Mechanics*, **238**, 57-64

23. Tsuji Y., Kawaguchi T., Tanaka T., 1993, Discrete particle simulation of two-dimensional fluidized bed, *Powder Technology*, **77**, 79-87

24. Valentik L., Whitmore R.L., 1965, The terminal velocity of spheres in Bingham plastics, *British Journal of Applied Physics*, **16**, 1197-1203

25. Yao L.M., Xiao Z.M., Liu J.B., Zhang Q., Wang M., 2020, An optimized CFD-DEM method for fluid-particle coupling dynamics analysis, *International Journal of Mechanical Sciences*, **174**, 105503

Manuscript received November 22, 2021; accepted for print April 21, 2022